Available online at www.sciencedirect.com
SCIENCE DIRECT®
Journal of Nuclear Materials 328 (2004) 21–30
journal of nuclear materials
www.elsevier.com/locate/jnucmat

Investigation of physico-mechanical properties of ceramic oxide kernels for nuclear applications

M.M. Titov *, J. Fachinger, A.A. Bukaemskiy

Institut für Sicherheitsforschung und Reaktortechnik, Forschungszentrum Jülich GmbH, D-52425 Jülich, Germany

Received 3 December 2003; accepted 23 February 2004

Abstract

In the present work, two different classes of oxide kernels were investigated: unirradiated thoria, urania and $(Th,U)O_2$ fuel kernels and low-density Al_2O_3 kernels for the incorporation of minor actinides. The physical mechanism of oxide kernel failure under uniaxial compression was investigated. A new method for determining the physico-mechanical properties of kernels has been developed and the parameters P_S and δ, characterising the level of stress required for destruction of the material structure and the brittleness of the investigated materials, respectively, were evaluated and discussed. It was shown that the value of P_S is analogous to traditional characteristics of material such as microhardness *Hv*. The 'quantisation' effect was revealed in the kernel crushing strength and deformation distributions. The physico-mechanical properties of ceramic kernels (average particle size, microstructure, phase state, density, P_S and δ) were investigated and comparative analysis of different kernel types was performed. Additionally, the impact of annealing time on the properties of low-density Al_2O_3 kernels was examined.

1. Introduction

Small kernels out of UO_2 and $(Th,U)O_2$ with a relation of Th/U of about 10:1 were used as nuclear fuel for high-temperature nuclear reactors (HTR) [1]. About 1 million spent fuel pebbles, each containing some ten thousands of fuel kernels, were produced during the operation of thorium high-temperature reactor (THTR 300) and experimental nuclear reactor (AVR). After the long interim storage period, it is planned to store the fuel elements in deep geological formations [2]. Therefore, the properties of these kernels are important with respect to the safety assessment of the final repository.

New applications of HTR are the objective of several projects in the 5th Framework Programme of the EU. The coated particles with mixed oxide (MOX) fuel kernels with reprocessed plutonium or minor actinides are investigated in order to reduce the toxicity potential during disposal by means of transmutation in HTRs [3,4]. Since the coated particles and ceramic fuel kernels are physically and chemically stable, they would be very suitable for eventual geologic disposal after appropriate conditioning. Recently, plutonia kernels were proposed for potential use in advanced radioisotope heater units and radioisotope power systems [5].

Kernels are small spherical particles with a diameter of a few hundred micrometers. Traditionally polycrystalline oxide kernels are produced by a modification of sol–gel technology [1,6,7]. After the stage of chemical synthesis, the produced particles are annealed at different temperatures depending on their subsequent applications. Fuel kernels are sintered at high temperatures (about 1600 °C) to form a dense polycrystalline material. The kernels for the fixation of radionuclides are annealed at relatively low temperatures in order to obtain material with a vermicular structure, which has a high specific surface. After infiltration by solutions of the radionuclides, they are finally sintered at high temperatures.

During application kernels are exposed to considerable external impacts, such as high temperatures,

* Corresponding author. Tel.: +49-2461 61 6523; fax: +49-2461 61 2450.
E-mail address: m.titov@fz-juelich.de (M.M. Titov).

0022-3115/$ - see front matter © 2004 Elsevier B.V. All rights reserved.
doi:10.1016/j.jnucmat.2004.03.001

mechanical stresses, irradiation and interaction with chemically aggressive media. Operation of kernels under such extreme conditions determines the necessity of comprehensive examination of their physico-mechanical properties.

Usually the kernels are characterised by the particle sizes, density, microstructure and phase state. However, using only the characteristics listed above does not provide complete information about the physico-mechanical properties of materials. For instance, the state and quality of grain boundaries remain unexplored. However, this parameter significantly determines material strength, crack-resistance and stability under exposure to aggressive media, which is important for nuclear applications.

The fact that kernels are in between powder and compact materials complicates the investigations. Many traditional methods of physico-mechanical and strength property investigation, such as microhardness measurements, bending strength, etc., are not applicable to kernels due to their small size and spherical shape.

It seems that the only mechanical characteristic of kernels which has ever been measured is the crushing strength of kernels under uniaxial compression [7–9]. However, in their works authors use only the average values of the crushing strength, which certainly does not only depend on material properties, but also on the particle size, loading conditions and hardness of measuring equipment. As a consequence, this value is practically inapplicable for the comparative analysis of different kernels. Furthermore, we are unfamiliar with any work investigating the mechanism of kernel failure in details.

In the present work, the results of investigating the physico-mechanical properties of different kernel types are presented. The physical mechanism of kernel failure under uniaxial compression was investigated. The method for determining the physico-mechanical properties of oxide kernels has been developed and new values for such a characterisation are proposed.

2. Materials and investigation methods

In the present work, two different classes of oxide kernels were investigated: unirradiated HTR thoria, urania and MOX fuel kernels and low-density Al_2O_3 kernels as a potential matrix for the incorporation of minor actinides. All investigated kernels have a regular spherical shape (Fig. 1(a)) and diameter in the range from 0.38 to 0.64 mm for the different kernel types (see Table 1).

Four different types of kernels on the basis of thoria and urania were investigated – ThO_2, $(Th_{0.906},U_{0.094})O_2$, $(Th_{0.834},U_{0.166})O_2$ and UO_2. The kernels have a polycrystalline structure with an average grain size of about 10 μm (Fig. 1(b)). The relative densities (ρ_r) measured by the hydrostatic weighing in water are about 98% of the

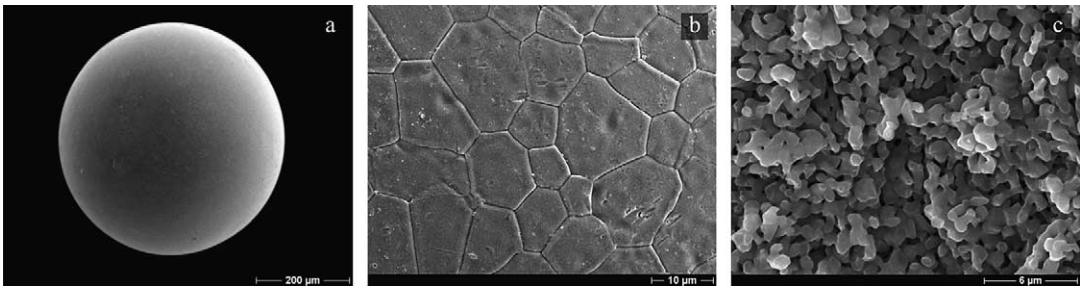

Fig. 1. SEM photograph of kernel F-0 (a), surface structure of F-100 (b) and fracture surface of A-0 (c).

Table 1
Parameters of different kernel types

Sample	Composition	Additional annealing	ρ_r (%)	$\langle d_0 \rangle$ (mm)
A-0	Al_2O_3	–	~61	0.64 ± 0.02
A-1	Al_2O_3	1 h, 1500 °C	~70	0.61 ± 0.02
A-3	Al_2O_3	3 h, 1500 °C	~74	0.60 ± 0.02
A-7	Al_2O_3	7 h, 1500 °C	~77	0.59 ± 0.02
A-Sint	Al_2O_3	5 h, 1600 °C	~96	0.56 ± 0.02
F-0	ThO_2	–	98 ± 2	0.50 ± 0.01
F-9.4	$(Th_{0.906},U_{0.094})O_2$	–	98 ± 2	0.61 ± 0.02
F-16.6	$(Th_{0.834},U_{0.166})O_2$	–	98 ± 2	0.38 ± 0.02
F-100	UO_2	–	98 ± 2	0.50 ± 0.01

theoretical density. The XRD analysis shows that the kernel material has a fluorite-type cubic structure and in the case of mixed oxide kernels represents a solid solution of ThO_2 and UO_2. Later for convenience of notification, the notation 'F-X' will be used, where X is the molar fraction of UO_2 in the material.

The initial alumina kernels have a vermicular structure with a characteristic constituent size of about 0.5 μm (Fig. 1(c)), which is common for oxide materials produced by different chemical methods (sol–gel, co-precipitation, etc.) and annealed below the sintering temperature. The relative density estimated by the geometrical method is about 61% of theoretical density.

To investigate the influence of temperature treatment on morphological structure and physico-mechanical properties, the Al_2O_3 kernels were additionally annealed at 1500 °C for 1, 3 and 7 h in air. The annealing leads to a decrease of kernel size and, therefore, to an increase of their relative density up to 77% of theoretical density. It is accompanied by increase of characteristic constituent size, decrease of pore sizes and their localisation. High-temperature sintering at 1600 °C for 5 h leads to an increase of the material relative density up to 96% of the theoretical density. After high-temperature sintering the Al_2O_3 kernels have an average grain size of about 16 μm and the morphological structure is similar to the structure of kernels F-X (Fig. 1(b)).

The XRD analysis shows that the material of the Al_2O_3 kernels is in the stable crystalline modification – α-Al_2O_3. Later the notation of 'A-X' will be used for these kernel types, where X is the time of additional annealing at 1500 °C. Additionally, the notation A-0 corresponds to the initial kernels, A-Sint – to the kernels after high-temperature sintering at 1600 °C.

The summary of different kernel type parameters are presented in Table 1.

The investigations of kernel mechanical properties were carried out by a universal machine for testing mechanical properties 'Instron-5544' with 50 N load cell. To provide the point loading of hard ceramic samples the work faces of the upper punch and specimen stage were fabricated from high-density alumina (99% of the theoretical density). The work faces were polished by a set of diamond polishing pastes down to 1 μm. The experimental scheme is presented in Fig. 2.

During the test procedure the kernel was placed between the work faces (Fig. 2) and loaded at a constant rate of 2 μm/s until failure. The distance between the work faces d was calculated from the position of the load cell considering the compression ratio of the measuring equipment. The diameter of kernel d_0 was measured as the distance between the work faces at the moment of their contact with the sample. At the moment of failure the force (crushing strength, F_C) and the maximal kernel deformation (Δd_C) were recorded (Fig. 3).

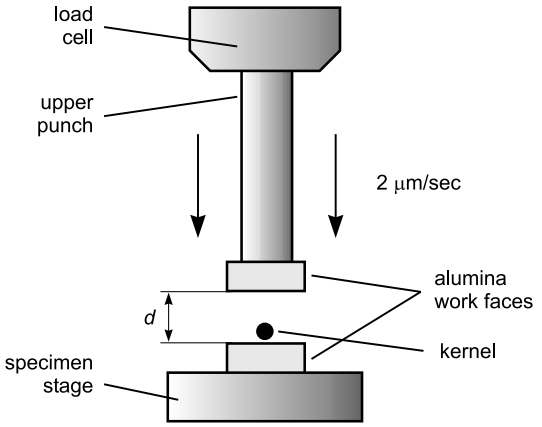

Fig. 2. Experimental scheme.

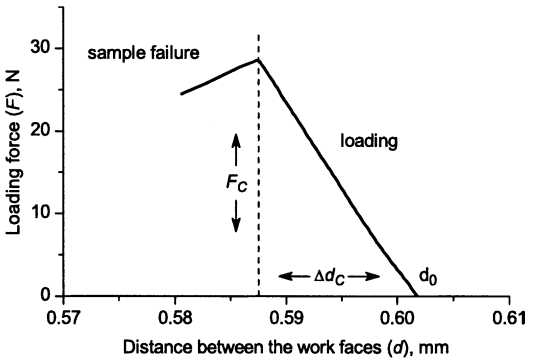

Fig. 3. Typical dependence of the distance between the work faces on the loading force.

For the statistical evaluation of experimental data more than 150 and 250 kernels of each type were tested for radioactive and non-radioactive materials, respectively. For each kernel type the following average values were determined: the diameter of the kernels $\langle d_0 \rangle$, the crushing strength $\langle F_C \rangle$ and the maximal kernel deformation $\langle \Delta d_C \rangle$. Moreover, the kernel crushing strength distribution histograms were investigated.

The morphological peculiarities of kernel structures were investigated by a scanning electron microscope (SEM) 'JEOL JSM-840'. For the investigations of material destruction character by SEM the samples were fixed on the special aluminium holders and loaded up to different loading forces.

3. Results and discussion

3.1. Physico-mechanical properties of kernels

The decrease of brittle sample size under compression occurs due to the elastic deformation and due to the destruction of material at the points of the force

application accompanied by the formation of so-called contact spots. However, our estimations of the elastic deformation level and the experimentally determined values of $\Delta d_C/d_0$ allow us to conclude that the decrease of kernel size under loading occurs mainly by the second mechanism.

Taking into account that kernel deformation $\Delta d \ll d_0$, the diameter of the contact spot (d_S) and its surface area (S_S) can be estimated from the geometrical considerations as follows:

$$d_S = \sqrt{2d_0\Delta d}, \tag{1}$$

$$S_S = \frac{\pi}{2} d_0 \Delta d. \tag{2}$$

The investigations of the kernel failure process were conducted by SEM. The formation of the round contact spots (Fig. 4(a)) was observed at the points of the force application. The contact spot diameters measured by the SEM photographs conforms to the values calculated by Eq. (1). For instance, after application of the loading force of 0.7 $\langle F_C \rangle$ to kernels A-3 the diameter of the contact spot was equal to 118 μm (calculation) and to about 120 μm (SEM measurements). For kernels F-9.4 it was equal to 76 μm and about 72 μm, respectively. This fact proves the appropriateness of our assumption that kernel deformation is mainly due to the destruction of the material in the points of the force application.

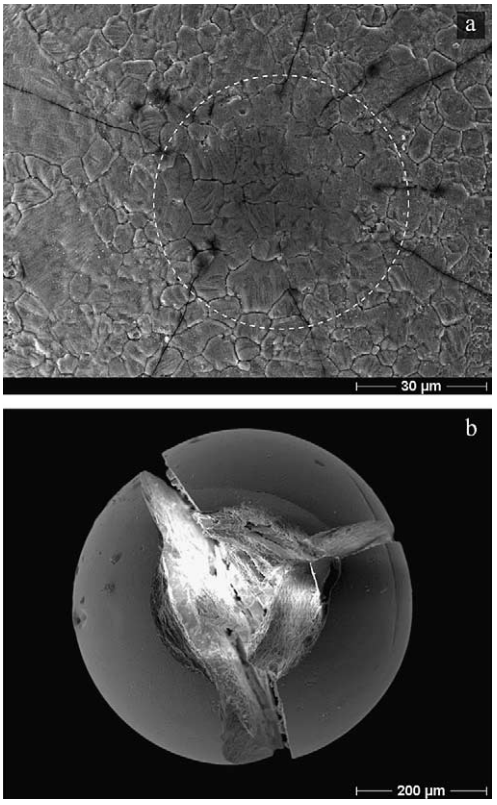

Fig. 4. Contact spot of F-16.6 (a) (shown by dashed line) and fragments of F-0 (b).

It was observed that a number of radial cracks are created around the contact spot boundary during loading (Fig. 4(a)). The contact spot boundary and cracks pass through the material independently of the grain boundaries and porous disposition (Fig. 4(a)). This indicates that the indentation of material under the contact spots occurs uniformly and is not influenced by the configuration of the material constituent.

When the loading force achieves its critical value (F_C) the brittle failure of the sample into radial fragments occurs (Figs. 4(b) and 5(a)). The fragments represent the regular spherical segments without that part of the material under the contact spots, which crumbles partially or completely at the moment of failure.

The SEM investigations show that material in these zones was destroyed during loading. This fact may be clearly demonstrated on kernels A-X, Fig. 5(b). In comparison to the original kernel material, which has a vermicular structure (Fig. 1(c)), material in destroyed zones consists of densely packed separate particles. The material destruction of kernels A-X occurs mostly by the interparticle joints, while for the kernels F-X it is preformed by the uniform crushing of grains.

The presence of the destroyed densified material under the contact spots can be explained in the following way. Material that has been placed 'above' the contact spots before loading is indented into the sample. As a consequence, the destruction of the structure and densification of material under the contact spots occurs. The profile of this zone can be reconstructed by the shape of the surviving sample fragments (Figs. 4(b) and 5(a)). It can be seen that the zone of destroyed densified material goes into the sample from the contact spot boundary and has a regular round shape symmetrical to the axis of loading.

Let us assume that the material in this zone is densified close to the density of a monolith. Therefore, one can use the reflection coefficient of $\rho_r/(1-\rho_r)$ to the material, indented inside the kernel, for the estimation of the depth of the destroyed densified material zone $h(r)$ at a distance r from the centre of the contact spot

$$h(r) = \frac{\rho_r}{2(1-\rho_r)}\left(\sqrt{d_0^2 - 4r^2} + \Delta d - d_0\right). \tag{3}$$

The profiles of the destroyed densified material zones were calculated at the moment of failure by Eq. (3) and are presented in Fig. 6. For these calculations the real sample parameters were used. It can be seen that for the dense samples F-X this zone has an elongated shape and depth, comparable to the kernel radius. On the contrary, for the low-density kernels A-X the zone of destroyed

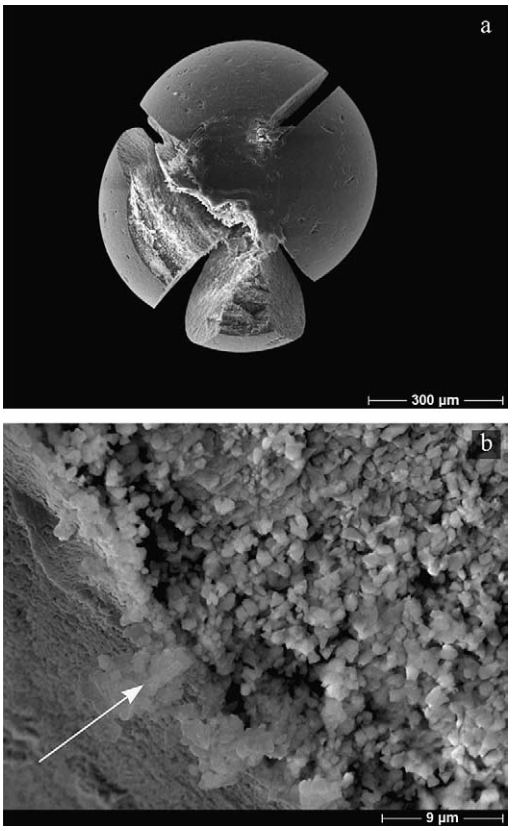

Fig. 5. Fragments (a) and destroyed densified material structure of A-3 (b) (the surface of the contact spot is shown by an arrow).

densified material is located mostly in the near-surface region.

The increase of the loading force is accompanied by the enlargement of the amount of material indented into the sample, which leads to an increase of depth of the destroyed densified material zone. This destroyed material uniformly transfers the loading pressure from the surface of the contact spot to the whole interface of the 'destroyed densified material–kernel'. This results in the creation of disjoining forces, initiation of the radial cracks and to further failure of the sample into the radial fragments (Figs. 4 and 5).

At the same loading force the disjoining force (F_r) may vary significantly in different samples due to different shapes of the destroyed densified material zone, depending on the material properties. The ratio (f_r) of the disjoining force to the loading force (F) can be calculated on the basis of Eq. (3)

$$f_r = \frac{F_r}{F} = \frac{\rho_r}{(1-\rho_r)}\left[\frac{d_0^2}{d_S^2}\arcsin\left(\frac{d_S}{d_0}\right) - \sqrt{\frac{d_0^2}{d_S^2}-1}\right]. \quad (4)$$

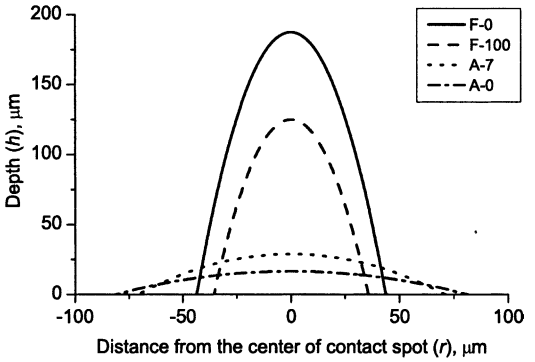

Fig. 6. Typical profiles of destroyed densified material zones.

The calculation of the f_r coefficient shows that the disjoining force at the moment of failure of kernels F-X exceeds the loading force by a factor of 4.7–5.8. Under the same conditions the f_r coefficient for kernels A-X is about one order of magnitude lower and is equal to 0.27–0.54.

It should be stated that for all kernel types the distance between the work faces (d) changes linearly with the loading force F (Fig. 3). In addition, the surface area (S_S) of the contact spot has a linear dependence on kernel deformation (Δd) (see Eq. (2)). Therefore, the pressure on the surface of the contact spot remains constant during the whole loading process and can be calculated as

$$P_S = \frac{F(d)}{S_S(d)} = \frac{2}{\pi d_0}\left|\frac{\partial F}{\partial d}\right| = \text{const.} \quad (5)$$

Because the pressure on the contact spot surface is constant, it can also be calculated from the parameters measured directly at the moment of failure

$$P_S = \frac{F_C}{S_S} = \frac{2}{\pi d_0}\frac{F_C}{\Delta d_C}. \quad (6)$$

The pressure P_S is an important structure-sensitive property of material. It characterises the level of stress required for destruction of material structure that conforms to our SEM investigation of the destroyed densified material zone.

The certain analogy between measuring methods for pressure P_S and the microhardness Hv is evident. In the experimental procedure proposed in the present work the destroyed densified material zone under the contact spot indents into the sample and plays the role of indenter. The surface area of the contact spot corresponds to some extent to the area of indentation during microhardness measurements. On the other hand, there is a significant difference between these methods. In our case the indentation is realised by the material itself instead of an external indenter. Moreover, the shape of the

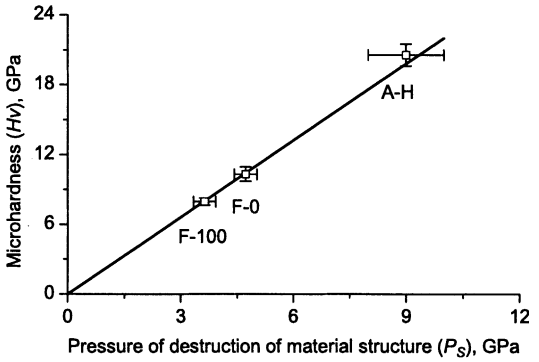

Fig. 7. Correlation between the pressure P_S and microhardness.

'indenter' is not the same for different objects and is determined by the properties of the tested materials.

It should be noted that the applicability of microhardness measurements for the ceramic spherical particles is limited by the small particle sizes and the complications of sample preparation, while the measurements of P_S are specially adapted for such purposes and require no additional sample treatment.

The correlation between the pressure P_S and literature data of the microhardness [10] is shown in Fig. 7. It can be seen that this correlation can be well fitted by a linear dependence of Hv on P_S, which starts from the zero point and has a slope of 2.3. To all appearance, the proportionality coefficient between Hv on P_S is defined by the geometry of measurements, the sample and indenter shapes and other experimental conditions.

The average values of the investigated characteristics for all kernel types are presented in Table 2. The values of P_S for the kernels A-X are sufficiently low, which is determined by their low relative density and a vermicular structure. The additional annealing leads to an increase of the relative density, material recrystallisation, crystallite growth, decrease and localisation of pores. The increase of density from 61% to 77% of theoretical density is accompanied by the increase of P_S from 1.1 to 2.4 GPa. The high-temperature sintering at 1600 °C (5 h) forms a polycrystalline material structure in kernels A-Sint. The estimated value of P_S increases in this case to approximately 9.0 GPa.

The values of P_S for the thoria and urania kernels are higher than for the low-density Al_2O_3 kernel, but significantly lower than for samples A-Sint. For the mixed oxide kernels F-9.4 and F-16.6 they are close (~4.0 GPa) and are between the values for the pure F-0 and F-100 (4.7 and 3.6 GPa, respectively).

The pressure P_S distribution (Fig. 8) for all kernel types has a single maximum and fits well by the Gaussian distribution (Fig. 8). The standard deviations from the average values are presented in Table 2.

Thus, the pressure P_S characterises the material structure of the investigated object and can be appropriately used for the comparative analysis of different sample materials.

On the contrary, the value of F_C characterises the investigated object as a whole and depends not only on material properties but also on other sample parameters. This value can only be used for the comparative analysis of objects which have a similar diameter and values of Δd_c. For instance, it can be successfully used for investigating the influence of the annealing process on the

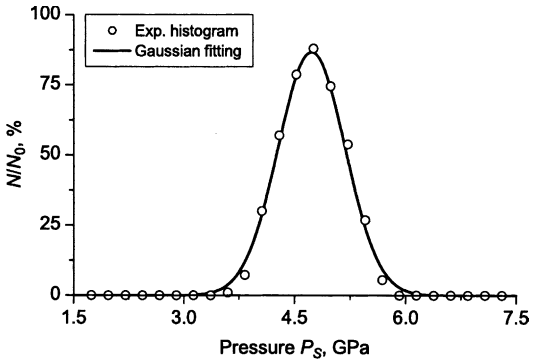

Fig. 8. The pressure P_S distribution for kernels F-0.

Table 2
Physico-mechanical properties of kernels investigated

Sample	$\langle F_C \rangle$ (N)	$\langle \Delta d_C/d_0 \rangle$ (%)	$\langle P_S \rangle$ (GPa)	Hv (GPa) [10]
A-0	20.0 ± 4.0	2.9 ± 0.5	1.1 ± 0.3	–
A-1	26.6 ± 5.1	2.8 ± 0.5	1.7 ± 0.4	–
A-3	32.6 ± 6.0	2.7 ± 0.4	2.1 ± 0.5	–
A-7[a]	37.5 ± 8.6	2.8 ± 0.5	2.4 ± 0.6	–
A-Sint[b]	>50	–	~9.0 ± 1.0	20.55 ± 0.95
F-0[a]	32.3 ± 7.6	1.54 ± 0.13	4.7 ± 0.3	10.31 ± 0.62
F-9.4	25.8 ± 3.4	1.14 ± 0.11	4.0 ± 0.4	–
F-16.6	13.8 ± 1.9	1.45 ± 0.21	4.0 ± 0.6	–
F-100	14.8 ± 1.5	1.03 ± 0.10	3.6 ± 0.3	7.95 ± 0.28

[a] Part of the kernels have a crushing strength of more than 50 N (see Table 3).
[b] For the calculation of P_S the deformation of the work faces was considered because of high sample hardness.

properties of Al_2O_3 kernels. Whereas for the samples which do not satisfy this condition such a comparison is not correct.

3.2. Kernel crushing strength and deformation distributions

During the investigations of the kernel crushing strength distribution histograms an interesting feature was noted. For all samples the distribution histograms have pronounced maximums at some values F_C (Fig. 9). This fact indicates that kernel failure occurs mainly at fixed values of the loading force.

For the statistical evaluation of experimental data, the kernel crushing strength distribution histograms were deconvolved onto separate significant peaks, which were fitted by Gaussian distribution. The parameters of Gaussian distribution for each peak (position of maximum F_{Ci}, variance σ_i, and peak area I) were determined from the demand for the minimum of the root-mean-square deviation of summary distribution from the experimental histogram. The number of significant peaks varies from six to nine for different kernel types.

The parameters of the experimental histogram evaluation for all kernel types are presented in Table 3. For a typical histogram, its deconvolution and summary distribution are shown in Fig. 9. It can be seen that the summary distribution coincides with the experimental histogram.

During processing of the histograms it was noted that the peaks of each histogram are almost equidistant. To prove this fact all peaks were numbered and the dependence of the peak positions F_{Ci} on their ordering numbers was evaluated by the least-squares method

$$F_{Ci} = ai + b, \tag{7}$$

where a is the distance between adjacent peaks, $(a + b)$ is the position of the first peak and i is the peak ordering number.

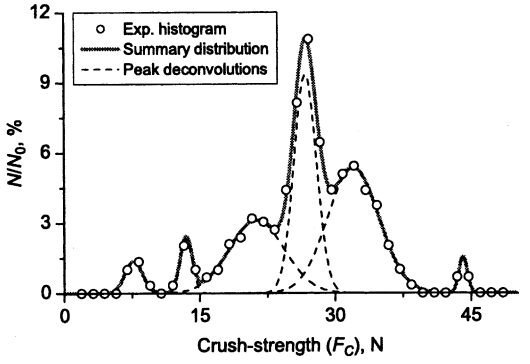

Fig. 9. The kernel crushing strength distribution for kernels A-1.

The ordering of peaks does not always start from 1. The condition that the value of b should be positive and less than the value of a was selected as a criterion. Such an approach ensures that peak number 1 (not always present in the distribution) always has the minimum crushing strength value. Dependences of F_{Ci} on peak ordering numbers and their linear fittings for all kernel types are presented in Fig. 10. In all cases the value of determination coefficient R^2 was not less than 0.99.

Peaks of kernels A-X have the ordering numbers 1–7. The dynamics of distribution with annealing time is shown in Fig. 11. Additional annealing leads to an increasing interpeak distance (a) and, therefore, to a shift of all peaks to the higher crushing strength values. This fact results in an increase of the F_{Ci} line slope from 4.5 to 7.4 N. Furthermore, a peak widening process takes place during annealing. For kernels A-0 the values of σ vary from 0.7 to 2.7 N and increase with annealing time up to 1.2–3.1 N for A-7. It should be noted that the peaks in the distributions of kernels A-X have significantly different variances.

Peaks of kernels F-X have the ordering numbers 4–14 and the values of σ range from 0.3–0.5 for kernels F-16.6 up to 0.6–1.1 for kernels F-0. No significant difference in peak variances within each distribution was observed.

It should be stated that the kernel deformation distribution is similar to the kernel crushing strength distribution, because the loading force is proportional to the change of sample size. In the present work we operate mostly in terms of loading force, because the precision of the force measurements are significantly higher than the precision of determining the distance between the work faces. The distance between adjacent peaks in the kernel deformation distribution can be calculated from parameter a as

$$\Delta d_a = a\left\langle \left| \frac{\partial F}{\partial d} \right| \right\rangle^{-1}. \tag{8}$$

Thus, the kernel failure occurs at fixed values of kernel deformation with the characteristic step Δd_a. The presence of this 'quantisation' was revealed for all types of investigated objects independently of their physico-mechanical properties, in particular independent of the type of microstructure (vermicular or polycrystalline) and geometrical characteristics of samples.

This effect can be explained in the following way. During the loading process around the destroyed densified material zone a number of radial cracks are initiated (Fig. 4(a)). The subsequent crack extension leads to an increase of their depth and at certain moment to sample failure. Due to the high symmetry of the samples and loading conditions all cracks can be assumed to be similar. Evidently, the more cracks are created the more the sample can be deformed before failure. Thus, the

Table 3
Parameters of peaks in the kernel crushing strength distribution

Sample	Peak No (i)	1	2	3	4	5	6	7	8	9	10	11	12	13	14	Out	a (N/peak)	b (N)	$\delta \times 10^3$
A-0	F_{Ci} (N)	6.5	12.1	16.5	19.8	24.4	30.0										4.5	2.4	6.2
	I (%)	3.9	11.1	7.5	39.8	36.3	1.3												
	σ (N)	0.7	1.8	1.1	1.7	2.7	0.8												
A-1	F_{Ci} (N)	7.7	13.5	21.3	26.7	32.0		44.1									6.1	2.0	6.2
	I (%)	3.3	3.9	23.7	29.3	38.0		1.8											
	σ (N)	1.0	0.7	3.0	1.2	2.8		0.5											
A-3	F_{Ci} (N)	8.6	14.3	21.2	30.3	35.9	43.4	49.1									7.1	0.8	5.8
	I (%)	1.5	3.3	9.2	40.7	27.9	14.5	3.0											
	σ (N)	0.8	0.8	2.1	2.3	1.6	2.6	0.8											
A-7	F_{Ci} (N)	11.1	17.2	26.0	36.1	41.4	46.1									>50	7.4	3.9	5.5
	I (%)	5.5	5.0	11.2	32.6	22.0	10.5									13.2			
	σ (N)	3.1	1.5	3.1	2.7	1.2	1.3												
F-0	F_{Ci} (N)						18.0	20.6	23.7	27.1	29.7	32.5	35.4	38.0	41.1	>50	2.9	0.7	1.5
	I (%)						2.0	8.3	16.3	10.8	18.7	19.3	4.7	3.0	3.0	13.8			
	σ (N)						0.6	0.8	1.0	0.9	0.8	1.1	0.8	0.9	0.6				
F-9.4	F_{Ci} (N)				13.0	16.3	19.7	22.8	26.0	28.8	32.3	35.7					3.2	0.3	1.4
	I (%)				2.7	2.0	5.4	24.8	22.6	32.6	8.8	1.1							
	σ (N)				0.9	0.6	0.9	1.0	0.8	1.0	1.0	0.9							
F-16.6	F_{Ci} (N)				5.8			10.0	11.4	12.8	14.4	15.9	17.2		19.6		1.4	0.2	1.5
	I (%)				2.3			4.3	12.8	28.0	26.5	13.2	11.6		1.4				
	σ (N)				0.3			0.3	0.4	0.4	0.5	0.4	0.4		0.3				
F-100	F_{Ci} (N)						10.7	12.2	13.7	15.7	17.2	19.0					1.7	0.5	1.2
	I (%)						2.3	8.4	41.1	29.8	16.5	1.8							
	σ (N)						0.4	0.6	0.7	0.6	0.4	0.6							

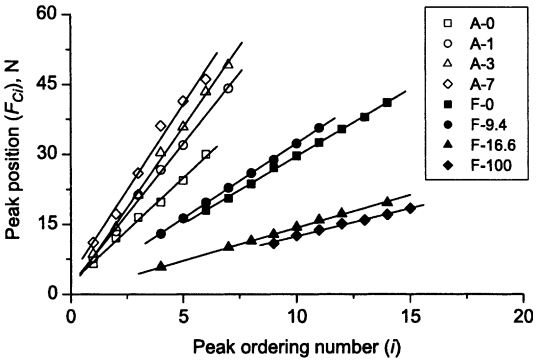

Fig. 10. Dependences of peak position on ordering number.

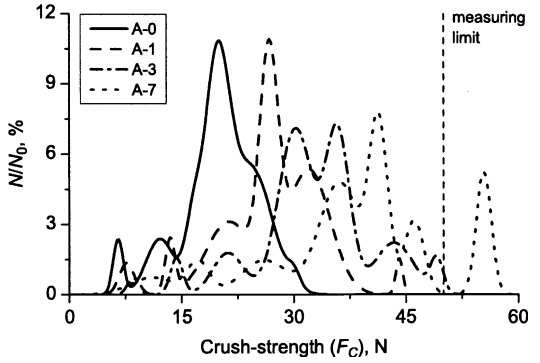

Fig. 11. Dynamics of the kernel crushing strength distribution with sintering time for kernels A-X.

reason for the 'quantisation' effect is the presence of a countable set of similar cracks.

Apparently, the ordering number of peak (i), to which the sample belongs, correlates to the number of cracks found in this sample at the moment of failure. Therefore, the 'quantisation' step Δd_a determines the sample deformation by initiation and extension of one crack. The constancy of the value of Δd_a results from the similarity of all the cracks in the sample.

This model of kernel failure can be indirectly confirmed by the following experimental finding. Visual inspection of cracked kernels showed that kernels F-X fail in more separate fragments than kernels A-X. It is logical to assume that the more cracks are created in the sample up to the moment of failure on the more fragments the sample fails. Indeed, as shown in Table 3 and Fig. 10, the peaks of kernels F-X have higher ordering numbers (i) than those of kernels A-X.

To exclude the influence of the sample size on the value of Δd_a the normalised characteristic deformation (δ) was calculated from Eqs. (8) and (5) as

$$\delta = \frac{\Delta d_a}{d_0} = \frac{2a}{\pi d_0^2 \langle P_S \rangle}. \quad (9)$$

The deformation δ characterises to some extent the brittleness of the investigated materials. This value decreases with increasing material brittleness and can be used for comparative analysis of different kernel types.

The values of δ for different samples are presented in Table 3. It can be seen that the value of δ for alumina kernels decreases with increasing annealing time from 6.2×10^{-3} for kernels A-0 to 5.5×10^{-3} for kernels A-7. The values of δ for kernels F-X are in the range from 1.2×10^{-3} to 1.5×10^{-3}, which is significantly lower than for alumina kernels. This fact demonstrates the much higher brittleness of dense kernels on the basis of thoria and urania than of low-density alumina kernels.

4. Conclusion

In the present work the physical mechanism of the failure of small spherical brittle particles (oxide kernels) under uniaxial compression was investigated. It was shown that during loading the formation of zones of destroyed densified material takes place under the contact spots. This results in the creation of disjoining forces, initiation of the radial cracks and to further failure of the sample into radial fragments.

A new method for determining the physico-mechanical properties of kernels has been developed and the values of P_S and δ introduced for such a characterisation.

The pressure on the contact spot surface (P_S), which characterises the level of stress required for destruction of material structure, was proposed for the analysis of kernel materials. It was shown that the value of P_S is to some extent analogous to such traditional characteristics of material as microhardness Hv.

The presence of the 'quantisation' effect was revealed in kernel crushing strength and deformation distributions. It was shown that the reason for the 'quantisation' effect is the presence of different numbers of similar cracks in the sample at the moment of failure. From the parameters of the 'quantisation' the value of normalised characteristic deformation (δ) was introduced. This value characterises the brittleness of the investigated materials to some extent.

The physico-mechanical properties of ceramic kernels (average particle size, microstructure, phase state, density) were examined. The values of pressure P_S and δ were determined for all kernel types. A comparative analysis of physico-mechanical properties of different kernel types was performed. Additionally, the impact of annealing time on the properties of low-density Al_2O_3 kernels was examined.

Acknowledgements

The FZJ team in charge of this sub-project wants to give thanks to the European Commission for

supporting this work. Contract No. FIKI-CT-2000-00020.

References

[1] H. Nickel, H. Nabielek, G. Pott, A.W. Mehner, Nucl. Eng. Des. 217 (2002) 141.
[2] N. Kirch, H.U. Brinkmann, P.H. Brucher, Nucl. Eng. Des. 121 (1990) 241.
[3] A. Baxter, C. Rodriguez, Prog. Nucl. Energy 38 (2001) 81.
[4] H.J. Rutten, K.A. Haas, Nucl. Eng. Des. 195 (2000) 353.
[5] M.S. El Genk, J.M. Tournier, Nucl. Eng. Des. 208 (2001) 29.
[6] H.D. Ringel, E. Zimmer, Nucl. Technol. 45 (1979) 287.
[7] G. Brambill, P. Gerontop, D. Neri, Energia Nucleare 17 (1970) 217.
[8] G. Ledergerber, F. Ingold, R.W. Stratton, H.P. Alder, C. Prunier, D. Warin, M. Bauer, Nucl. Technol. 114 (1996) 194.
[9] C. Ganguly, H. Langen, E. Zimmer, E.R. Merz, Nucl. Technol. 73 (1986) 84.
[10] Physico-Chemical Properties of Oxides, Reference book under the editorship of G.V. Samsonov, Metallurgy, Moscow, 1969.